

The Role of Hydrogen and Oxygen Interstitial Defects in Crystalline Si cells: Mechanism of Device Degradation in Humid Environment

Bo Li,^a Feifei Zhang,^b Yu Pang,^a Huiyan Zhao,^b Guocai Liu,^a Chao He,^{*a} and Xingtao An^{*a}

^aSchool of Science, Hebei Provincial Key Laboratory of Photoelectric Control on Surface and Interface, Hebei University of Science and Technology, Shijiazhuang, 050018, Hebei, China

^bDepartment of Physics and Hebei Advanced Thin Film Laboratory, Hebei Normal University, Shijiazhuang, 050024, Hebei, China.

ABSTRACT: The efficiency of silicon solar cells gradually decreases in various environments, with humidity being a key factor contributing to this decline. This study investigates the humidity-induced failure mechanisms in crystalline silicon solar cells. Using density functional theory and the non-equilibrium Green's function method, we systematically examine the microscopic diffusion mechanisms of hydrogen and oxygen defects and their impact on photovoltaic performance. Hydrogen and oxygen are interstitial defects that can introduce both deep-level and resonant-state recombination centers, thereby reducing carrier lifetime and solar cell efficiency. Furthermore, hydrogen exhibits prominent diffusion pathways, particularly in its +1 and 0 charge states at the BC site ($H_{i(BC)}^{+1}$ and $H_{i(BC)}^0$), while oxygen in its +1 and 0 charge states shows a higher diffusion barrier at the BC1 site ($O_{i(BC1)}^{+1}$ and $O_{i(BC1)}^0$). These defects, induced by moisture and temperature fluctuations, exacerbate the degradation of solar cell performance. By analyzing these defect behaviors, this research provides valuable insights into the failure mechanisms of Si solar cells, especially under humid conditions.

1. INTRODUCTION

Renewable energy sources are increasingly preferred due to their environmental sustainability. Among these, solar cells are widely used devices for harnessing renewable energy, with crystalline silicon (c-Si) solar cells dominating the market and accounting for 80% of the share¹. Compared to other types, such as perovskite and thin-film cells, c-Si solar cells offer significant advantages, including superior stability and higher conversion efficiency². Despite their high stability, the efficiency of c-Si solar cells gradually declines over time due to prolonged use and environmental factors. Various methods, including light aging and damp heat tests, have been employed to investigate the causes of this efficiency decline³⁻⁵. Several degradation mechanisms, including light-induced degradation (LID)⁵, potential-induced degradation (PID)⁶ and Humidity-induced degradation (HID)⁷, are considered to be the most prominent factors affecting performance during operation^{8, 9}.

HID involves the detrimental effects of moisture on solar cell materials, primarily by accelerating defect formation and diffusion, which in turn degrades cell performance⁷. This is especially concerning given the ubiquitous presence of water in natural environments, which exacerbates the degradation process. Water is a common external factor for silicon solar cells under natural conditions. HID in c-Si solar cells is closely linked to the deterioration of encapsulation materials, such as ethylene-vinyl acetate (EVA) films. Over time, experiments have demonstrated that prolonged exposure to moisture induces corrosion and oxidation of EVA, while temperature fluctuations promote condensate formation within the cells or encapsulation layers, ultimately resulting in dampness and accelerating the degradation process¹⁰. Water penetrating the solar cell through the back sheet interacts with the SiO₂/Si interface, where Si dangling bonds facilitate the formation of an SiO₂/Si layer¹¹. The reaction between water and Si ultimately leads to the formation of individual hydrogen atoms¹². These hydrogen atoms can then diffuse into the silicon lattice along the vacant sites of the silicon crystal. Hydrogen interstitial defects could also arise in c-Si during the crystal growth process¹³. These hydrogen-induced defects may significantly impair battery performance, and their removal from crystalline materials is virtually impossible¹³⁻¹⁶.

Oxygen atoms can infiltrate c-Si through the SiO₂/Si interface, facilitated by the presence of OH⁻, H₂O, and H₃O⁺¹². This infiltration occurs as oxygen atoms break Si-O bonds in the SiO₂

structure and disrupt O-O pairs, leading to the dissociation of these species. Once oxygen enters the SiO₂ layer, it typically remains there due to the high energy barrier (approximately 2.5 eV) for further dissociation. Additionally, c-Si inherently contains an interstitial oxygen concentration of approximately 10¹⁸ cm⁻³¹⁷. Oxygen's behaviour in silicon, including its tendency to occupy fewer interstitial sites¹⁸⁻²⁰ and form thermal donors¹⁹ under elevated temperatures, significantly influences the electronic properties of silicon, thereby enhancing carrier recombination and contributing to efficiency losses in solar cells.

Although substantial research has focused on the infiltration of hydrogen and oxygen into the silicon surface, the microscopic mechanisms governing the migration of these interstitials within silicon and their impact on photovoltaic performance remain largely unexplored. Understanding these atomic-level processes is crucial for investigating HID. To address this gap, the present study examines the microscopic behaviour of hydrogen and oxygen defects in c-Si under humid conditions, systematically assessing their impact on the performance of silicon-based solar cells. This study employs Density Functional Theory (DFT), Climbing Image Nudged Elastic Band (CI-NEB) methods, and quantum transport theory to explore the behavior of hydrogen and oxygen, as well as their radicals, within the c-Si lattice. The primary objective is to understand how these species contribute to the failure mechanisms of silicon solar cells, particularly in humid environments. By elucidating the microscopic mechanisms of defects in c-Si solar cells, this research provides valuable insights into the degradation of efficiency in practical applications.

2. METHODS

2.1 Details for DFT calculations

The structures were optimized using the Vienna Ab Initio Simulation Package (VASP)²¹, a software based on the plane-wave pseudopotential method that solves the Kohn-Sham equations²¹ to determine the ground-state electronic structure of materials. The generalized gradient approximation²² (GGA/PBE) for the exchange-correlation functional was applied to ensure accurate energy calculations and optimized geometries for the systems under investigation. After obtaining the optimized structures, single-point energies were calculated to evaluate the electronic properties at specific configurations. The VASP parameters for the c-Si

supercell containing 64 atoms included a plane wave cutoff energy of 450 eV and a $2 \times 2 \times 2$ k-point grid. The electronic and ionic convergence criteria were set to 1.56×10^{-9} eV/atom and 10^{-5} eV/Å, respectively. Calculations were performed in $2 \times 2 \times 2$ supercells to minimize finite size effects, and all atoms in the supercell were allowed to relax. All calculations were carried out in reciprocal space.

2.2 Formation energies

The formation energies of defects were calculated following the method outlined in the literature, identifying the defects that are most readily formed²³. Additionally, the formation energies²⁴ of defects with different charge states as a function of the Fermi level were also determined.

$$\Delta H_f(X_i^q) = E(\text{Si}_N X; q) - E(\text{Si}_N) - n\mu_X + q(E_{\text{VBM}} + E_F) - E_{\text{corr}} \quad (1)$$

Here, $E(\text{Si}_N)$ represents the total energy of the pristine crystal containing N Si atoms. $E(\text{Si}_N X; q)$ denotes the total energy of the crystal containing a defect X with charge state q , where X represents either an oxygen or hydrogen interstitial defect. μ_X is the chemical potential of defect X , and n denotes the number of defects. E_{VBM} represents the energy of the valence band maximum (VBM), while E_{corr} refers to the correction term in the defect formation energy.

This highlights the need to carefully consider the limitations and potential errors associated with simulating charged defects in finite-sized supercells, as the primary source of E_{corr} arises from electrostatic interactions between mirror charges. In DFT calculations, finite-sized supercells are typically used to model defects. Due to the finite size of the supercell, charged defects induce electrostatic interactions between the defect and its periodic images, leading to errors in the calculated energies. The Makov-Payne correction method^{25, 26} is employed to account for these interactions, specifically E_{corr} , which includes both the leading electrostatic interaction and higher-order correction terms. The detailed calculation formula is given in formula S (1), while formula (2) provides an approximate formula. The energy is calculated using the following formula:

$$E_{\text{corr}} = \frac{q^2 \alpha}{2\epsilon L} \quad (2)$$

The correction term was computed using equation (2), with the specific values provided in Tables 1 and 2.

Table 1 The correction values E_{corr} for the formation energies of hydrogen interstitial defects were calculated using the Makov-Payne correction method

H SITES	Corrected energy for different H charge states (eV)	
	+1	-1
T	0.02	0.02
BC	0.02	0.02
C	0.02	0.02
M	0.02	0.02
H	0.02	0.02
AB	0.02	0.02

Table 2 The correction values E_{corr} for the formation energies of oxygen interstitial defects were calculated using the Makov-Payne correction method

O SITES	Corrected energy for different O charge state (eV)			
	+2	+1	-1	-2
BC1	0.05	0.02	0.02	0.05

2.3 Chemical potential

After addressing the defect formation energies and their correction terms, the discussion transitions to the construction and analysis of chemical potential phase diagrams, which offer further insights into the thermodynamic stability of defects. The atomic chemical potential is defined as²³:

$$\mu_X = E_X + \Delta\mu_X \quad (3)$$

Here, E_X represents the reference energy per atom of X in its natural state. For hydrogen, E_H is the energy per atom in H_2 , and for oxygen, E_O is the energy per atom in O_2 .

The following secondary items should not be considered for precipitation: SiH_4 、 Si_2H_6 、 H_2 、 SiO 、 SiO_2 、 SiO_4 、 O_2 , as these compounds are all in the gaseous state. Additionally, since the study focuses on the behavior of individual interstitial defects within the crystal, it is crucial to establish the chemical potential ranges, which can be determined using the following calculation formula.

$$\Delta\mu_{Si} + 4\Delta\mu_H < \Delta H(SiH_4) = -9.41 \text{ eV} \quad (4)$$

$$2\Delta\mu_{Si} + 6\Delta\mu_H < \Delta H(Si_2H_6) = -14.13 \text{ eV} \quad (5)$$

$$\Delta\mu_H \leq 0 \quad (6)$$

$$\Delta\mu_{\text{Si}} + \Delta\mu_{\text{O}} < \Delta\text{H}(\text{SiO}) = -1.28\text{eV} \quad (7)$$

$$\Delta\mu_{\text{Si}} + 2\Delta\mu_{\text{O}} < \Delta\text{H}(\text{SiO}_2) = -3.11\text{eV} \quad (8)$$

$$\Delta\mu_{\text{Si}} + 4\Delta\mu_{\text{O}} < \Delta\text{H}(\text{SiO}_4) = -1.92\text{eV} \quad (9)$$

$$\Delta\mu_{\text{O}} \leq 0 \quad (10)$$

$$\Delta\mu_{\text{Si}} > 0 \quad (11)$$

2.4 CI-NEB

The CI-NEB²⁷ method was used to calculate the diffusion barriers of hydrogen and oxygen in different charge states within c-Si. The magnitude of the diffusion barrier primarily depends on the configuration of the host crystal during the diffusion process. Both the Nudged Elastic Band (NEB)²⁸ and CI-NEB methods are employed to calculate the minimum energy path (MEP) between two stable states, which are commonly used to study reaction pathways and transition states. NEB optimizes a set of intermediate images along the path but may converge to incorrect transition states, particularly in complex energy landscapes. This limitation arises because NEB does not specifically target the highest energy image, leading to inaccuracies in transition state identification. In contrast, CI-NEB improves upon NEB by allowing the highest energy image to "climb" up the potential energy surface, ensuring that it corresponds to the correct transition state. This makes CI-NEB more reliable for accurately identifying transition states and handling complex energy profiles, especially in systems with multiple saddle points. However, CI-NEB requires more computational resources due to the climbing procedure. Overall, while NEB is computationally simpler, CI-NEB provides a more accurate and robust solution for systems where precise transition state identification is crucial.

2.5 Photocurrent

To provide a clearer understanding of the impact of interstitial defects at different sites on the photocurrent of Si-based solar cells, a device was constructed using (100) Si with and without interstitial hydrogen or oxygen defects. The device consists of a left lead (L), a central region (CR), and a right lead (R), as shown in Fig. S1. Subsequently, the Atomistix Tool Kit (ATK) software²⁹, based on DFT combined with the non-equilibrium Green's function (NEGF) method³⁰, was used to compute the photovoltaic current. This method allows for the simulation of electronic transport properties under non-equilibrium conditions. The combination of VASP for structural optimization and ATK for transport properties enables a comprehensive analysis of

the photovoltaic performance at the atomic level.

All DFT+NEGF calculations in this study were performed using the ATK software, which used the GGA+1/2 exchange-correlation method³¹ and Perdew-Burke-Ernzerhof (PBE) functional³². The photocurrent was then calculated as a first-order perturbation to the device's electronic system by introducing the electron-photon interaction Hamiltonian³³.

$$H' = \frac{e}{m_0} \mathbf{A} \cdot \mathbf{P} \quad (12)$$

Where \mathbf{A} is the vector potential for a monochromatic light and \mathbf{P} is the momentum operator.

$$\mathbf{A} = \mathbf{e} \left(\frac{h\sqrt{\tilde{\mu}_r \tilde{\epsilon}_r}}{4\pi N\omega c \tilde{\epsilon}} F \right)^{\frac{1}{2}} (be^{i\omega t} + b'e^{-i\omega t}) \quad (13)$$

where $\tilde{\mu}_r$ is relative permeability, $\tilde{\epsilon}_r$ is the relative permittivity, ω is the light frequency, F is the photon flux, N is the number of photons, b and b' represent the bosonic annihilation and creation operators, respectively. In this work, $\tilde{\epsilon}_r = 13.1$ was adopted, based on first-principles calculations, and a photon flux F of $1\text{s}^{-1}\text{\AA}^{-2}$. The polar light energy ranged from 0 to 5.5eV.

The perturbation Hamiltonian H' can be added to the central region Hamiltonian H_{CR} for the next DFT+NEGF calculations using open boundary conditions along the photocurrent direction. The Hamiltonian H_{L} for left lead and H_{R} for right lead can be computed using periodic boundary conditions within the DFT framework. In the entire device calculations above, the k point's mesh was set as $3 \times 3 \times 87$ to ensure the energy convergence to be $1 \times 10^{-5}\text{eV/atom}$. Finally, the self-consistent spectral density matrix of the central region can be obtained:

$$\rho(E)^{\text{L(R)}} = \frac{1}{2\pi} G(E)\Gamma(E)^{\text{L(R)}}G^\dagger(E) \quad (14)$$

It includes electronic density contributions from both the left and right leads. The retarded Green's function matrix, $G(E)$, incorporates the effects of the lead states on the central region, referred to as the self-energy³⁶ $\Sigma(E)^{\text{L(R)}}$:

$$G(E) = [(E + i\delta_+)S - H_{\text{CR}} - \Sigma(E)^{\text{L}} - \Sigma(E)^{\text{R}}]^{-1} \quad (15)$$

where δ_+ is an infinitesimal positive number, and S represents the overlap matrix of the central region. The broadening function of the left (right) lead is given by:

$$\Gamma(E)^{\text{L(R)}} = i \left[\Sigma(E)^{\text{L(R)}} - \Sigma(E)^{\text{L(R)\dagger}} \right] \quad (16)$$

Then, the current into the left and right leads due to the absorption of photons is given by³⁵,

³⁶:

$$I_{\alpha} = \frac{e}{h} \int_{-\infty}^{+\infty} \sum_{\alpha, \beta=L,R} [1 - f_{\alpha}(E)] f_{\beta}(E - \hbar\omega) T_{\alpha, \beta}^{-}(E) - f_{\alpha}(E) [1 - f_{\beta}(E + \hbar\omega)] T_{\alpha, \beta}^{+}(E) dE \quad (17)$$

where f_{α} and f_{β} are the Fermi distribution functions of left and right leads. $T(E)$ is the transmission coefficient $T(E)$ is given by³⁷:

$$T(E) = \text{Tr}[\Gamma(E)^L G(E) \Gamma(E)^R G(E)^{\dagger}] \quad (18)$$

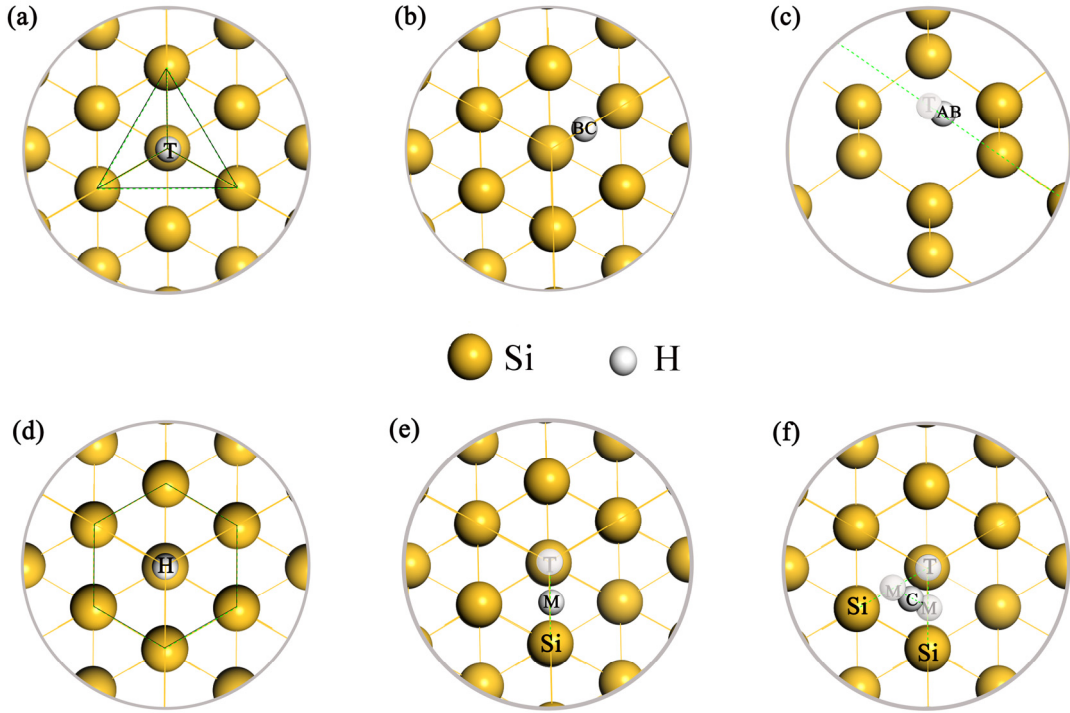


Figure 1 Interstitial hydrogen located at six high symmetry sites: T_d (the center of the space formed by the tetrahedron of the nearest four of Si atoms) (a)、 BC (Bond-Center) (b)、 AB (Anti-bonding) (c)、 H (Hexagonal) (d)、 M (Mid) (e) and C (Connecting) (f) within the c-Si.

3. Results and Discussion

3.1 Impact of H interstitial defects

The differences in spin properties between deuterium and hydrogen, along with the constraints of theoretical models, pose significant challenges to research^{13, 38-51}. A relatively clear conclusion regarding hydrogen's stable interstitial position in Si was not reached until 1994³⁹. Estreicher et al. identified six stable sites for hydrogen within (between two nearest Si atoms), shown in Fig. 1(b); AB ⁵³ (Anti-bonding, located along the $\langle 111 \rangle$ direction in the crystal, opposite to the Si-Si bond, 0.42 Å from the T_d site), shown in Fig. 1(c); H ⁵⁴ (Hexagonal, the

center of the hexagonal face formed by Si atoms), shown in Fig. 1(d); M⁴³ (Mid, the midpoint along the line connecting the T_d site and the nearest Si atom), shown in Fig. 1(e); and C⁴³ (the center of the line connecting two adjacent M sites), shown in Fig. 1(f).

Hydrogen atoms were placed in positions described in the literature^{48, 55}. Subsequently, relaxation and self-consistent calculations were performed in VASP for the three charge states (-1, 0, and +1) at the corresponding positions. After relaxation, it was observed that H_i⁺¹, initially positioned at the T_d and C sites, spontaneously relaxed to the BC site, as shown in Fig. S2. When analyzing H_{i(T_d)}⁺¹ and H_{i(C)}⁺¹, it can be considered as H_{i(BC)}⁺¹.

To investigate the electronic structure of the crystal, the energy band structure was calculated. The band structure was computed using the PBE functional, yielding a band gap of 0.57 eV, as shown in Fig. S3(a). Additionally, calculations using the HSE06 functional provided a band gap of 1.11 eV, which is consistent with literature values⁵⁶ (Fig. S3(b)). The band gap determined using HSE06 was then used to define the range of the electronic Fermi level in the defect formation energy calculations.

In Fig. 2(a), the black lines represent SiH₄, the blue lines represent Si₂H₆, and the AOCA region indicates the area where no secondary phase exists. The region above the diagonal line corresponds to where the secondary phase can precipitate, while the region below the diagonal line corresponds to where it cannot precipitate. When a hydrogen atom enters the Si lattice, the formation reaction between them is not considered. Therefore, the formation of two gaseous secondary phases, SiH₄ and Si₂H₆, at standard temperature and pressure should be excluded as constraints. The gray area in the figure represents the range of $\Delta\mu_{\text{H}}$ and $\Delta\mu_{\text{Si}}$ obtained from these constraints. In Fig. 2(a), it can be seen that $-\infty < \Delta\mu_{\text{H}} < -2.35$ eV, yielding a hydrogen rich value of -2.35 eV, while $\Delta\mu_{\text{Si}} > 0$. The obtained a hydrogen rich value here is a relative chemical potential. To obtain the absolute chemical potential, the energy of H must be added. $E_{\text{H}} = -1.12$ eV, resulting in a final rich H value of -3.47 eV. By substituting these values into formula (1), the defect formation energies for -1, 0, and +1 charge states at different sites near the Fermi level are obtained. As shown in Fig. S4, the most favorable sites for occupation are the T, BC, C, and H sites (with T and C sites being equivalent to the BC site). However, the path between two hydrogen atoms at hexagonal sites along the $\langle 111 \rangle$ crystal direction is too long to occur in practical scenarios and is thus not considered⁵⁴. The formation energies of all defects at all sites were calculated, and the H_{i(BC)}⁺¹ was found to be the most stable, with a formation energy

of -8.41 eV^{57} , as shown in Fig. S4. The diffusion barrier for $\text{H}_{i(\text{BC})}^{+1}$ to move between equivalent BC sites is 7.16 eV (Fig. S3(d)), indicating that diffusion is highly unlikely without external forces. For other charge states, $\text{H}_{i(\text{T})}^0$ and $\text{H}_{i(\text{BC})}^0$ exhibits lower formation energies, approximately -1.71 eV , as shown in Fig. S4(a) and (b).

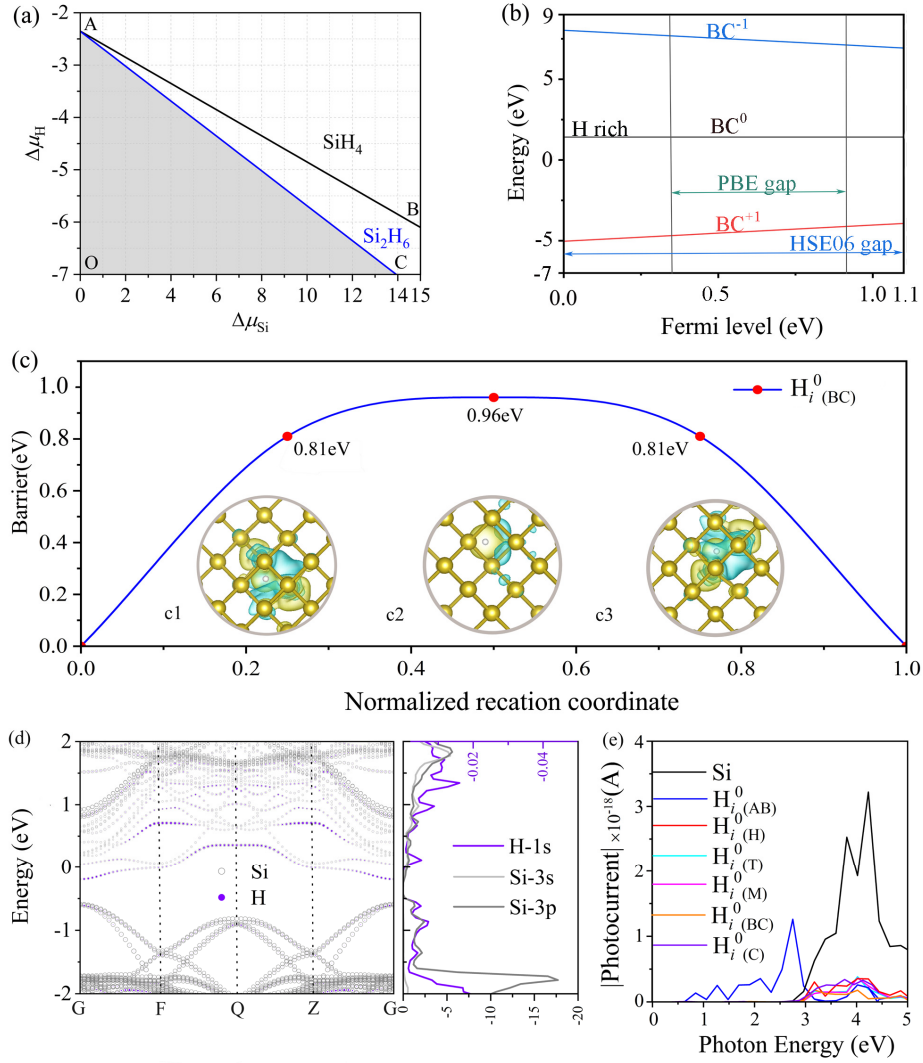


Figure 2 The chemical potential range for $\Delta\mu_{\text{Si}}$ and $\Delta\mu_{\text{H}}$ doping in the c-Si (a); the formation energies of $\text{H}_{i(\text{BC})}^{-1}$, $\text{H}_{i(\text{BC})}^0$ and $\text{H}_{i(\text{BC})}^{+1}$; (b); the diffusion barrier of the pathway for hydrogen from the BC site to the nearest BC site, along with the corresponding differential charge density for the diffusion path (c); and the combination of projected bands and projected density of states (d); photocurrent intensity figure of neutral hydrogen dopant defects at different sites (e).

To better understand the diffusion properties of hydrogen, the diffusion barrier for $H_{i(\text{BC})}^0$ and $H_{i(\text{T})}^0$ was also investigated. The diffusion barrier of $H_{i(\text{BC})}^0$ was calculated to be 0.96 eV, as shown in Fig. 2(c), which differs by 0.12 eV from the value of 0.84 eV reported by Dewar et al.^{13, 58}, who used the MINDO/3 method⁵⁹. The discrepancy between the diffusion barriers obtained from MINDO/3 and CI-NEB can be attributed to differences in methodological accuracy. MINDO/3, a semi-empirical method, often approximates electronic interactions, which may lead to lower accuracy in complex diffusion barrier calculations, especially when compared to more rigorous methods like CI-NEB. CI-NEB explicitly considers energy changes along diffusion pathways using first-principles calculations, making it generally more reliable for precise barrier height determination. Our results are consistent with experimental data, indicating that the diffusion of neutral hydrogen (H^0) at the BC site occurs readily. Additionally, our study found that the diffusion barrier of H^0 at the T-T site is 0.71 eV, as shown in Fig. S3(c). This suggests that while H^0 is not easily accommodated at the T site, it diffuses very easily once there. In addition, the diffusion barriers of M and C have also been studied, which are 26.85 eV and 7.16 eV, respectively, show as Fig. S6 (c) and (d).

According to Fig. S4, the formation energy of H_i^{-1} is significantly larger than H_i^0 , indicating that the H_i^{-1} cannot stably occupy any site within Si under spontaneous conditions. This suggests that, even without external influence, hydrogen atoms will spontaneously diffuse. The instability of H_i^{-1} in c-Si is evident, as it diffuses freely within the lattice. Such unrestrained diffusion implies that H_i^{-1} could disrupt the lattice structure, potentially influencing the crystal's electronic properties.

In Fig. 2 (c1-c3), the differential charge density plots (white represents hydrogen atoms and yellow represents Si atoms, with blue areas indicating electron flow toward Si atoms and yellow areas indicating electron flow toward hydrogen atoms) illustrate the diffusion of hydrogen. These plots show that the distribution of the electron cloud varies with the position of hydrogen. The interaction between the electron cloud distributions of silicon and hydrogen atoms highlights the critical role of Si-H electron sharing in determining hydrogen diffusion pathways within silicon. As hydrogen atoms migrate through the silicon lattice, their movement is influenced by how their electron clouds overlap with those of nearby silicon atoms, which shapes the spatial configuration and energetics of the diffusion process. Increased electron sharing enhances the interaction between hydrogen and silicon, creating a more favorable diffusion environment.

Consequently, the diffusion path from the BC site to the nearest BC site is identified as the most likely and energetically favorable within c-Si, aligning with the results reported by Walle et al.⁶⁰. This BC-BC path also corresponds with the literature description of the diffusion path BC-C(or M)-BC, as presented by Walle et al.⁶⁰, as shown in Fig. S3(d).

Fig. 2(d) shows the energy states present in the outermost 3s and 3p orbitals of Si and the 1s orbital of hydrogen near the Fermi level. It is evident that the hydrogen defect at the BC site lies 0.24 eV below the conduction band minimum (CBM). This suggests that hydrogen doping introduces a deep-level defect within the silicon crystal structure, classifying it as a carrier recombination center. Such deep-level defects can trap charge carriers, leading to increased non-radiative recombination rates, which, in turn, negatively affect the efficiency of silicon-based electronic devices, such as solar cells and transistors. By acting as a recombination center⁶¹, the hydrogen defect effectively reduces carrier lifetimes, hindering charge transport and overall device performance.

We also calculated the band structures at other sites. The results show that, even at different sites, hydrogen defects consistently manifest as harmful defects, either as deep-level or resonance states, as shown in Fig. S5. This demonstrates the universality of the detrimental effects of hydrogen defects across various sites, providing a more comprehensive theoretical foundation for understanding their impact on material properties.

To validate the above analysis, the photovoltaic current of hydrogen-doped silicon-based solar cells was calculated. The introduction of hydrogen defects into c-Si significantly impacts its photovoltaic properties, as shown in Fig. 2(e). Our calculations, based on quantum transport theory, reveal that hydrogen doping, regardless of the specific lattice site, leads to a significant reduction in photocurrent intensity. From Fig. 2(d) and Fig. 2(e), it is evident that the defect states introduced by hydrogen are deep-level defects and carrier recombination centers, which negatively affect the photoelectric performance of c-Si, substantially decreasing the photocurrent intensity. This decline suggests that hydrogen defects hinder the efficient transport of photo-generated charge carriers, which is crucial for optimal photovoltaic performance. In Si solar cells, maintaining high photocurrent efficiency is essential for effective energy conversion. Thus, the detrimental role of hydrogen defects implies disruption of charge carrier mobility and recombination processes, ultimately compromising the overall efficiency of c-Si in photovoltaic

applications. This also explains one of the reasons why water reduces the efficiency of silicon-based solar cells.

3.2 Impact of O interstitial defects

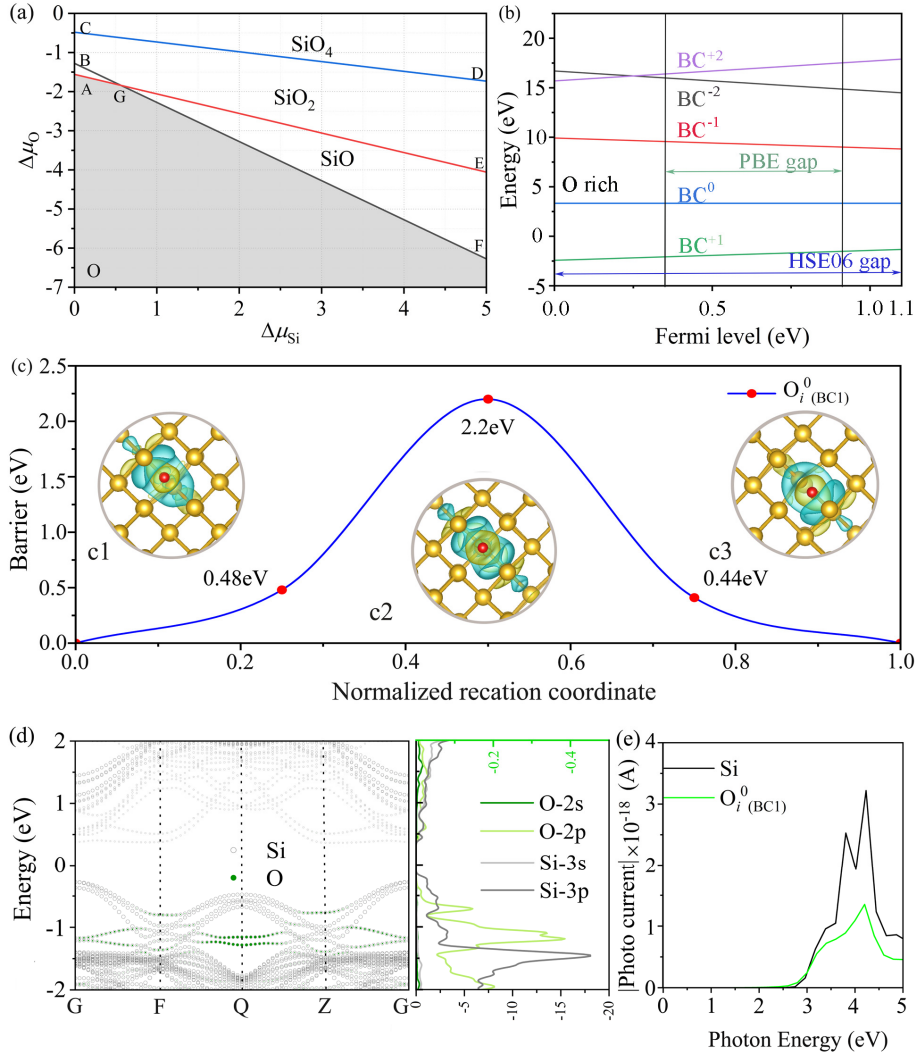


Figure 3 The secondary phases considered for oxygen (a) doping in the c-Si; the defect formation energies of $O_{i(BC1)}^{-2}$, $O_{i(BC1)}^{-1}$, $O_{i(BC1)}^0$, $O_{i(BC1)}^{+1}$, $O_{i(BC1)}^{+2}$ (b); the diffusion barrier of the pathway for oxygen from the BC1 site to the nearest BC1 site, along with the corresponding differential charge density for the diffusion path (c); and the combination of projected bands and projected density of states (d); photocurrent intensity figure of oxygen dopant defects at different sites (e).

To investigate the effects of interstitial oxygen defects with different oxidation states in c-Si, a similar methodology is employed. First, the range of the oxygen chemical potential within c-Si is considered to calculate the corresponding formation energies. This

chemical potential range is determined to prevent the precipitation of O₂ and the formation of Si-oxide phases (SiO, SiO₂, SiO₄), allowing for the construction of the $\Delta\mu_{\text{O}}$ (oxygen chemical potential) and $\Delta\mu_{\text{Si}}$ (silicon chemical potential), as shown in Fig. 3(a).

Figure 3(a) derives the chemical potential range for oxygen defects that prevents the precipitation of the aforementioned oxides: $-\infty < \Delta\mu_{\text{O}} < -1.56$ eV. The AGFHO region indicates the area where no secondary phase exists. The oxygen rich value is determined to be -1.56 eV (point A), which can be substituted into formula (1) to obtain the corresponding formation energy for oxygen interstitial defects. The obtained oxygen rich value here is a relative chemical potential. To obtain the absolute chemical potential, the energy of O must be added. $E_{\text{O}} = -4.93$ eV, resulting in a final rich O value of -6.94 eV.

Previous studies have shown that the occupancy site of interstitial oxygen in c-Si differs from that of hydrogen, as oxygen occupies only the BC site within Si^{19, 20}. There are six equivalent BC sites for oxygen in c-Si, all considered equivalent. Additionally, previous research¹⁴ indicates that during diffusion, oxygen prefers the BC1 site configuration, as shown in Fig. S7(a). Therefore, the initial and final states of diffusion can be studied at the BC1 site. The distance between O and the nearest Si atoms is 1.563 Å, and the Si-O-Si bond angle is 98°.

By substituting the previously determined oxygen-rich chemical potential value into formula (1), the formation energies for the five oxidation states of oxygen (-2, -1, 0, +1, +2) were obtained. These formation energies are plotted in Fig. 3(b). It is evident that oxygen interstitials in the +1 state are most likely to occupy BC sites and form defects within the crystal. Oxygen interstitials in the 0 state are also likely to occupy BC sites. Using the CI-NEB method, the diffusion barriers and pathways for oxygen interstitials in the +1 and 0 states between BC sites were calculated. The results show that the diffusion pathways for oxygen in both the +1 and 0 states are nearly identical, characterized by a semicircular diffusion path, as shown in Fig. S7(b). The diffusion pathway of oxygen atoms is asymmetric.

This finding aligns with conclusions from the literature¹⁴. The diffusion barrier for the oxygen atom with the +1 oxidation state (O_i^{+1}) is relatively high, reaching 7.71 eV, as shown in Fig. S7(b). This supports the understanding that lower formation energies correspond to higher mobility and lower barriers. In contrast, the diffusion barrier for $\text{O}_{i(\text{BC}1)}^0$, is lower, at only 2.2 eV,

as shown in Fig. 3(c). This suggests that external conditions, such as high temperature and pressure, can facilitate the diffusion of the oxygen atoms with the 0 oxidation state (O_i^0). Experimental observations indicate that most of the oxygen atoms observed are in the 0 oxidation state, which is linked to the lower diffusion barrier of these atoms¹⁹. Due to their lower formation energy and diffusion barrier, the oxygen atoms with the 0 oxidation state are more likely to form and diffuse, leading to increased mobility within c-Si and a higher probability of detection. In contrast, although the oxygen atoms with the +1 oxidation state are the easiest to form, they are relatively stable. Without focused attention on BC sites, their likelihood of detection is significantly lower than that of neutral oxygen atoms. As shown in Fig. 3(d), the oxygen defect at the BC1 site lies at the valence band edge. Theoretical and experimental studies have demonstrated that oxygen-related defects at the VB are resonance states that can capture charge carriers, thereby reducing device transport efficiency⁶². These defects introduce localized states within the band structure, significantly altering carrier dynamics. Resonant oxygen states near the valence band maximum (VBM) act as trap centers, affecting both hole and electron mobility by creating scattering centers that hinder free movement. This effect is particularly detrimental in devices where high carrier mobility is crucial, such as transistors and solar cells, as it leads to non-radiative recombination pathways that reduce overall device efficiency. Additionally, these defect-induced trapping mechanisms can increase recombination rates, limiting the lifetime of excited states and decreasing photocurrent in optoelectronic applications, as shown in Fig. 3(e)⁶³. Addressing these oxygen-related resonant states is therefore critical for enhancing material performance.

Conclusions

Both hydrogen and oxygen act as significant defects in c-Si, functioning as carrier recombination centers that substantially affect solar cell performance. HID exacerbates these effects by creating conditions that promote the activation and mobility of these defects, further impairing the operational stability and efficiency of solar cells. This study utilizes first-principles calculations to investigate the microscopic behaviors of hydrogen and oxygen atoms within the silicon lattice, focusing on their occupancy sites, diffusion pathways, and electronic characteristics. The results show that the H_i^{+1} , is the most readily formed defect, predominantly localized at the BC site. Additionally, H_i^0 , which

also tends to occupy the BC site, is identified as a deep-level defect. Notably, H_i^0 exhibit greater diffusivity, with a diffusion barrier of 0.96 eV, a process that is further enhanced under high humidity conditions. In contrast, oxygen atoms exhibit a diffusion barrier of 2.2 eV. Oxygen defects, which are characterized as resonant states, also function as carrier recombination centers, similar to hydrogen defects. Under humid conditions, the penetration of water molecules and the formation of condensates can destabilize the silicon lattice and increase the mobility of oxygen atoms, thereby amplifying their detrimental effects. These defects disrupt carrier lifetime and conductivity, while also significantly degrading the structural integrity of the silicon lattice. The interaction between HID and the diffusion and activation of these defects underscores the importance of addressing hydrogen- and oxygen-related degradation mechanisms. A comprehensive understanding of their diffusion pathways, charge states, and recombination mechanisms under humid conditions is crucial for developing strategies to mitigate HID, thereby improving the stability and performance of silicon-based solar cells in real-world environments.

Acknowledgements

This research was supported by National Science Foundation of China (No. 12074096 and No. 11747103), Science and Technology Project of Hebei Education Department (No. QN2022149) and Scientific Research Project of Universities in Hebei Province (JCZX2025023).

References

1. J. Kim, M. Rabelo, S. P. Padi, H. Yousuf, E. C. Cho, and J. S. Yi, *Energies* **2021**, *14* (14), 21.
2. M. Palsgaard, T. Markussen, T. Gunst, M. Brandbyge, and K. Stokbro, *Physical Review Applied* **2018**, *10* (1), 7.
3. C. Han, *Solar Energy Materials and Solar Cells* **2020**, *210*, 110488.
4. S. Kumar, R. Meena, and R. Gupta, *Solar Energy* **2019**, *194*, 903-912.
5. J. Lindroos, and H. Savin, *Solar Energy Materials and Solar Cells* **2016**, *147*, 115-126.

6. B. van der Zee, Y. Li, G.-J. A. H. Wetzelaer, and P. W. M. Blom, *Physical Review Applied* **2022**, *18* (6), 064002.
7. T. H. Kim, N. C. Park, and D. H. Kim, *Microelectronics Reliability* **2013**, *53*, 1823-1827.
8. A. Ndiaye, A. Charki, A. Kobi, C. M. F. Kébé, P. A. Ndiaye, and V. Sambou, *Solar Energy* **2013**, *96*, 140-151.
9. W. Luo, Y. S. Khoo, P. Hacke, V. Naumann, D. Lausch, S. P. Harvey, J. P. Singh, J. Chai, Y. Wang, A. G. Aberle, et al, *Energy & Environmental Science* **2017**, *10* (1), 43-68.
10. J. Yang, H. Fang, and Y. Gao, *Nano Energy* **2016**, *30*, 614-620.
11. D. J. Chadi, *Physical Review B* **2001**, *64* (19), 195403.
12. C. Y. Chang, C. Y. Lin, and D. S. Lin, *J. Phys.-Condes. Matter* **2021**, *33* (40), 8.
13. S. J. Pearton, J. W. Corbett, and M. Stavola, *Hydrogen in Crystalline Semiconductors*, 1991.
14. D. Colleoni, and A. Pasquarello, *Journal of Physics: Condensed Matter* **2016**, *28* (49), 495801.
15. R. Siddiqui, R. Kumar, G. K. Jha, G. Gowri, M. Morampudi, P. Rajput, S. Lata, S. Agariya, B. Dubey, G. Nanda, et al, *Energy* **2016**, *107*, 550-561.
16. C. G. Van de Walle, and B. R. Tuttle, *Ieee Transactions on Electron Devices* **2000**, *47* (10), 1779-1786.
17. Z. D. Zeng, J. D. Murphy, R. J. Falster, X. Y. Ma, D. R. Yang, and P. R. Wilshaw, *Journal of Applied Physics* **2011**, *109* (6), 10.
18. A. Borghesi, B. Pivac, A. Sassella, and A. Stella. *Journal of Applied Physics* **1995**, *77* (9), 4169-4244.
19. T. Y. Tan, *Applied Physics A* **1982**, *28*, 79-92.
20. T. Y. Tan and U. Gösele, *Diffusion in Semiconductors*, Springer Berlin Heidelberg, **2005**.
21. G. Kresse, *Physical Review B* **1996**, *54* (16), 169-186.
22. M. C. Payne, M. P. Teter, and D. C. Allan, *Reviews of Modern Physics* **1992**, *64* (4), 1045-1097.

23. C. Freysoldt, B. Grabowski, T. Hickel, J. Neugebauer, G. Kresse, A. Janotti, and C. G. Van de Walle, *Reviews of Modern Physics* **2014**, 86 (1), 253-305.
24. S.-H. Wei, *Computational Materials Science* **2004**, 30 (3-4), 337-348.
25. M. Leslie, and N. J. Gillan, *Physics C: Solid State Physics* **1985**, 18 (5), 973-982.
26. G. Makov, M. C. Payne, *Physical Review B* **1995**, 51 (7), 4014-4022.
27. G. Henkelman, B. P. Uberuaga, H. Jónsson, *The Journal of Chemical Physics* **2000**, 113 (22), 9901-9904.
28. G. Henkelman, H. Jónsson, *The Journal of Chemical Physics* **2000**, 113 (22), 9978-9985.
29. J. Schneider, J. Hamaekers, S. T. Chill, S. Smidstrup, J. Bulin, R. Thesen, A. Blom, and K. Stokbro, *Modelling and Simulation in Materials Science and Engineering* **2017**, 25 (8), 085007.
30. M. Brandbyge, J.-L. Mozos, P. Ordejón, J. Taylor, and K. Stokbro, *Physical Review B* **2002**, 65 (16), 165401.
31. L. G. Ferreira, M. Marques, and L. K. Teles, *Physical Review B* **2008**, 78 (12), 125116.
32. J. P. Perdew, K. Burke, and M. Ernzerhof, *Physical Review Letters* **1996**, 77 (18), 3865-3868.
33. L. E. Henrickson, *Journal of Applied Physics* **2002**, 91 (10), 6273-6281.
34. M. V. Bollinger, K. W. Jacobsen, and J. K. Nørskov, *Physical Review B* **2003**, 67 (8), 085401.
35. S.-L. Yu, and J.-X. Li, *Physical Review B* **2012**, 85 (14), 144402.
36. R. L. Cristian Rivas, Gerhard Klimeck, William R. Frensley, Massimo V. Fischetti, Phillip E. Thompson, Sean L. Rommel, and Paul R. Berger, *Applied Physics Letters* **2001**, 78 (6), 814-816.
37. N. Papior, N. Lorente, T. Frederiksen, A. García, and M. Brandbyge, *Computer Physics Communications* **2017**, 212, 8-24.
38. K. G. Nakamura, K. Ishioka, M. Kitajima, A. Endou, M. Kubo, and A. Miyamoto, *The Journal of Chemical Physics* **1998**, 108 (8), 3222-3225.
39. S. K. Estreicher, M. A. Roberson, and D. M. Maric, *Physical Review B* **1994**, 50 (23), 17018-17027.

40. M. Dürr, and U. Höfer, *Progress in Surface Science* **2013**, *88* (1), 61-101.
41. Y. B.-Y. Chris G. Van de Walk, and S. T. Pantelides, *Physical Review B* **1987**, *60* (26), 2761-2764.
42. A. Diggs, Z. Zhao, R. V. Meidanshahi, D. Unruh, S. Manzoor, M. Bertoni, S. M. Goodnick, and G. T. Zimányi, *Communications Materials* **2023**, *4* (1), 1-10.
43. P. Deák, L. C. Snyder, and J. W. Corbett, *Physical Review B* **1988**, *37* (12), 6887-6892.
44. K. J. Chang, and D. J. Chadi, *Physical Review B* **1989**, *40* (17), 11644-11653.
45. K. Inagaki, Y. Morikawa, H. Ohmi, K. Yasutake, and H. Kakiuchi, *Aip Advances* **2021**, *11* (8), 085318.
46. N. M. Johnson, *Journal of non-crystalline solids* **1991**, *137*, 11-16.
47. N. Martsinovich, A. L. Rosa, M. I. Heggie, C. P. Ewels, and P. R. Briddon, *Physica B: Condensed Matter* **2003**, *340*, 654-658.
48. S. K. Estreicher, *Materials Science and Engineering* **1995**, *17*, 319-412.
49. P. V. Santos, N. M. Johnson, R. A. Street, M. Hack, R. Thompson, and C. C. Tsai, *Physical Review B* **1993**, *47* (16), 10244-10260.
50. A. J. Morris, C. J. Pickard, and R. J. Needs, *Physical Review B* **2008**, *78* (18), 8.
51. C. O. Rodriguez, M. Jaros, and S. Brand, *Solid State Communications* **1979**, *31* (1), 43-45.
52. K. J. Chang, and D. J. Chadi, *Physical Review Letters* **1988**, *60* (14), 1422-1425.
53. C. H. Seager, R. A. Anderson, and D. K. Brice, *Journal of Applied Physics* **1990**, *68* (7), 3268-3284.
54. D. d. F. dell, U. d. Lecce, and V. Arnesano, *Solid State Communications* **1989**, *69* (3), 305-309.
55. J. W. Corbett, S. N. Sahu, T. S. Shi, and L. C. Snyder, *Physics Letters A* **1983**, *93* (6), 303-304.
56. M. L. Cohen, and T. K. Bergstresser, *Physical Review* **1966**, *141* (2), 789-796.
57. F. Buda, G. L. Chiarotti, R. Car, and M. Parrinello, *Physical Review Letters* **1989**, *63* (3), 294-297.
58. P. Deák, L. C. Snyder, J. L. Lindström, J. W. Corbett, S. J. Pearton, and A. J. Tavendale, *Physics Letters A* **1988**, *126* (7), 427-430.

59. M. J. S. Dewar, E. G. Zoebisch, E. F. Healy, and J. J. P. Stewart, *Journal of the American Chemical Society* **1985**, *107* (13), 3902-3909.
60. P. J. H. Denteneer, C. G. Van de Walle, and S. T. Pantelides, *Physical Review B* **1989**, *39* (15), 10809-10824.
61. R. Jones, B. J. Coomer, J. P. Goss, B. Hourahine, and A. Resende, *Solid State Phenomena* **1999**, *71*, 173-248.
62. M. Aghajanian, B. Schuler, K. A. Cochrane, J. H. Lee, C. Kastl, J. B. Neaton, A. Weber-Bargioni, A. A. Mostofi, and J. Lischner, *Physical Review B* **2020**, *101* (8), 6.
63. S. M. Sze, Y. Li and K. K. Ng. *Physics of semiconductor devices*. John wiley & sons, **2021**.

Supporting information for

The Role of Hydrogen and Oxygen Interstitial Defects in Crystalline Si

cells: Mechanism of Device Degradation in Humid Environment

Bo Li,^a Feifei Zhang,^b Yu Pang,^a Huiyan Zhao,^b Guocai Liu,^a Chao He^{*a} and Xingtao An^{*a}

^aSchool of Science, Hebei Provincial Key Laboratory of Photoelectric Control on Surface and Interface, Hebei University of Science and Technology, Shijiazhuang, 050018, Hebei, China

^bDepartment of Physics and Hebei Advanced Thin Film Laboratory, Hebei Normal University, Shijiazhuang, 050024, Hebei, China

Makov-Payne correction method:

The exact formula of Makov-Payne correction method is

$$E_{\text{corr}} = \frac{q^2\alpha}{2\varepsilon L} + \frac{2\pi qQ}{3\varepsilon L^3} - O(L^{-5}) \quad (1)$$

Here, q represents the defect charge, α is the Madelung constant, ε is the dielectric constant, L is the length of the crystal cell (typically taken as the diagonal length of the supercell), and Q is the electric quadrupole moment (a higher-order term that is usually negligible). For the last term $O(L^{-5})$, it denotes a correction term of the order L^{-5} , which is a higher-order correction considering the finite size effects of the supercell. This term diminishes as the supercell size increases and can thus be neglected in calculations. Therefore, when applying the Makov-Payne correction to defect formation energy, it is sufficient to calculate by the following formula:

$$E_{\text{corr}} = \frac{q^2\alpha}{2\varepsilon L} \quad (2)$$

In a supercell containing 64 atoms, $L = \sqrt{a^2 + b^2 + c^2} = 18.94 \text{ \AA}$. $\alpha = \sum_i \frac{1}{r_i}$ [1]

$$\alpha = 4 \times \frac{1}{0.214} - 12 \times \frac{1}{0.35} + 12 \times \frac{1}{0.41} = 18.69 - 34.28 + 29.26 = 13.67 \quad (3)$$

The dielectric tensor at each site was determined using VASP software, and the determinant was calculated to obtain ε .

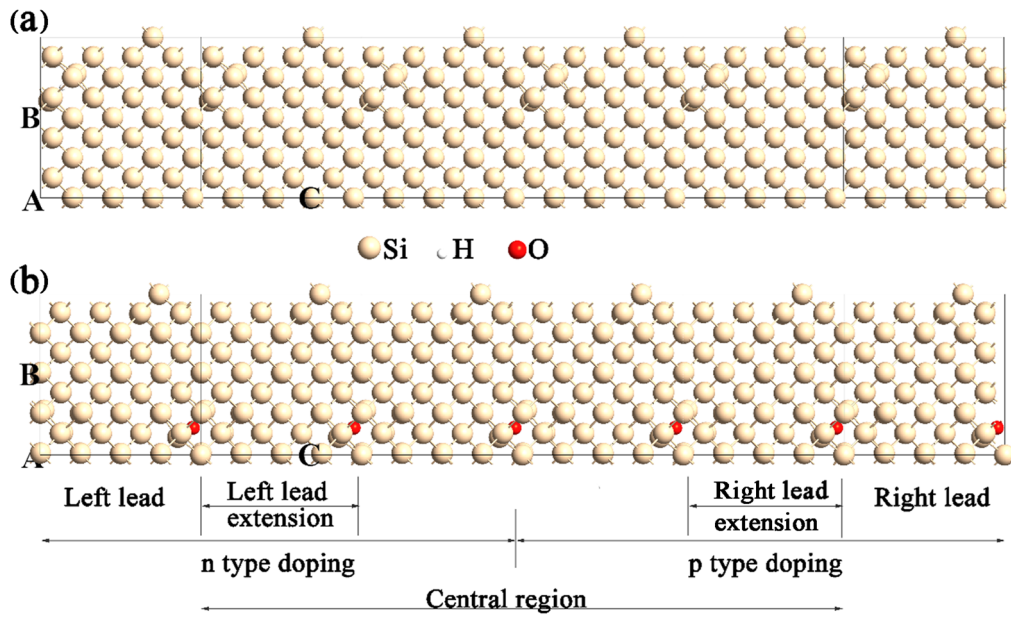


Figure S1. The architecture of the solar cell device based on H interstitial (BC site) (a), and O interstitial (BC1 site) (b). The left part and right part of the device are n type and p type separately, with doping level of $2 \times 10^{-19} \text{ e/cm}^3$.

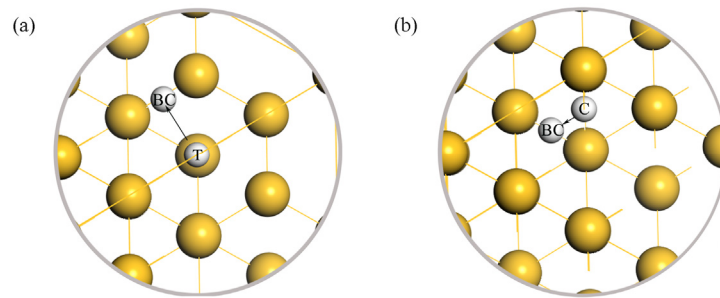


Figure S2. The position of Td^{+1} (a) and C^{+1} (b) site changed to BC after relaxation

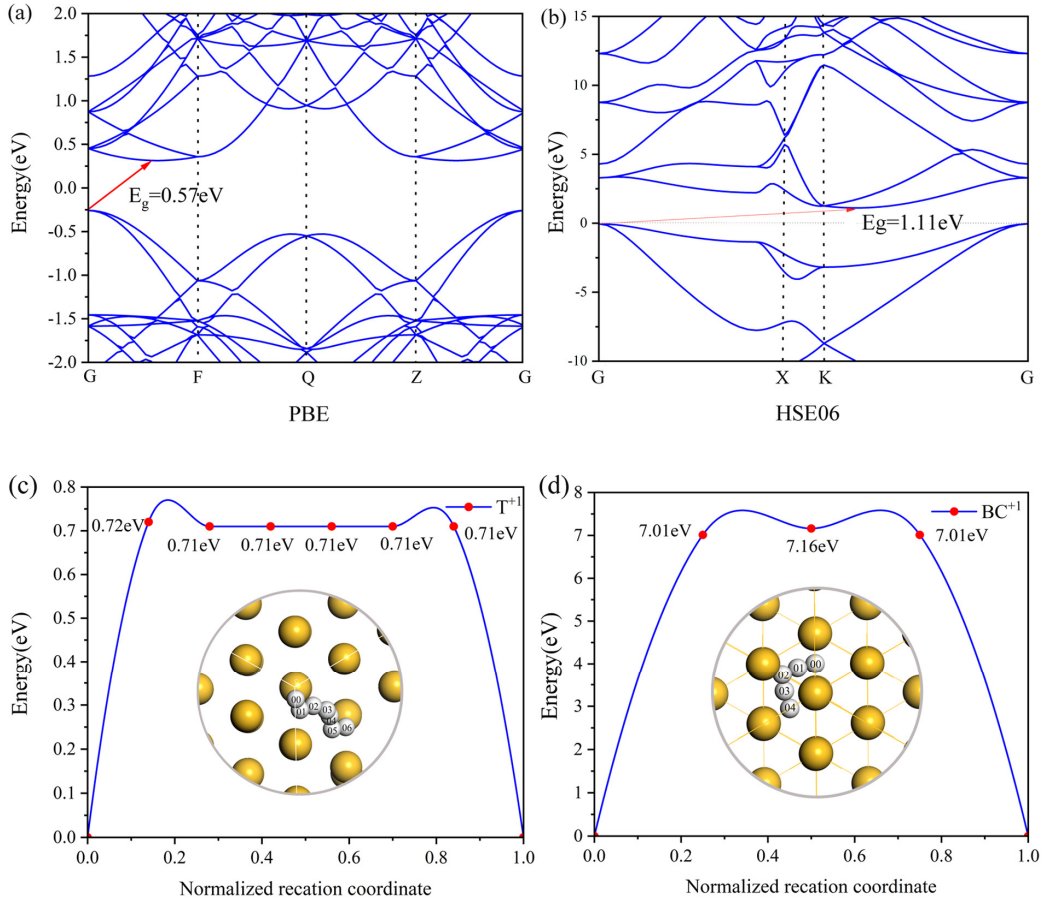


Figure S3. Band structure calculated using PBE (a) and HSE06 (b) of Si, and the diffusion barriers and diffusion pathways of +1 charged hydrogen at the T site (c) and BC site (d)

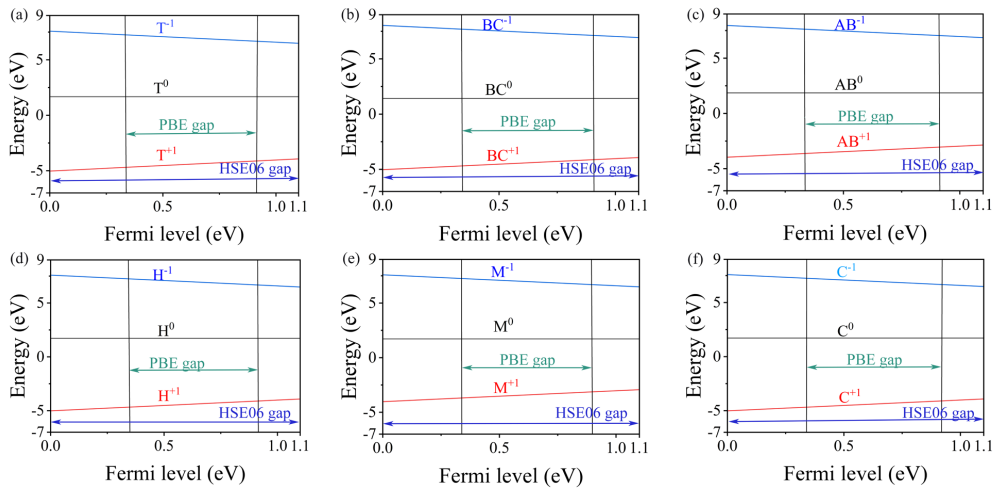


Figure S4 The formation energies of interstitial hydrogen at the T (a), BC (b), AB(c), H(d), M(e), C(f) for the charge states -1, 0, and +1.

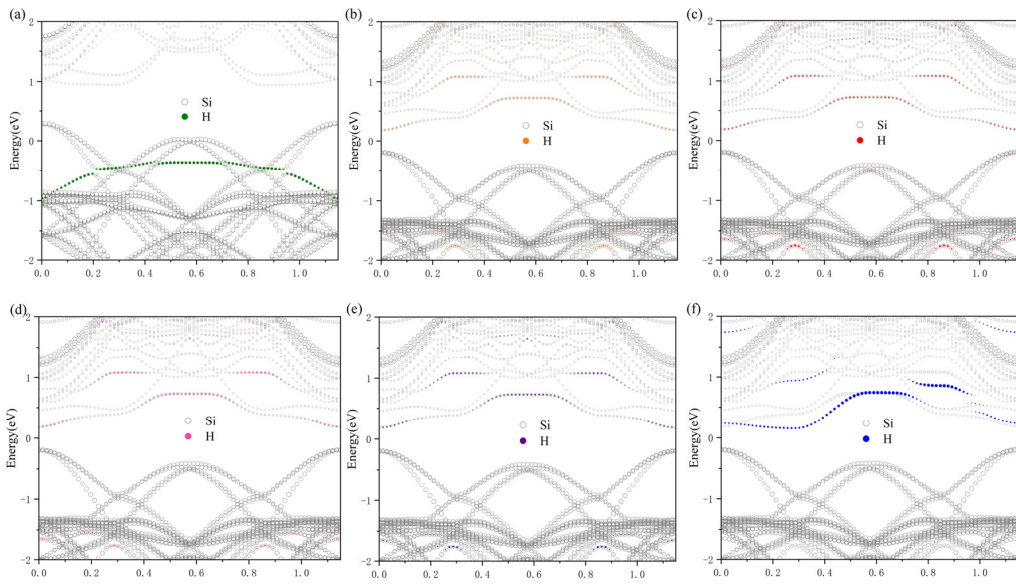


Figure S5 The band of interstitial hydrogen at T(a), BC(b), AB(c), H(d), M(e), C(f) for the +1 charge state

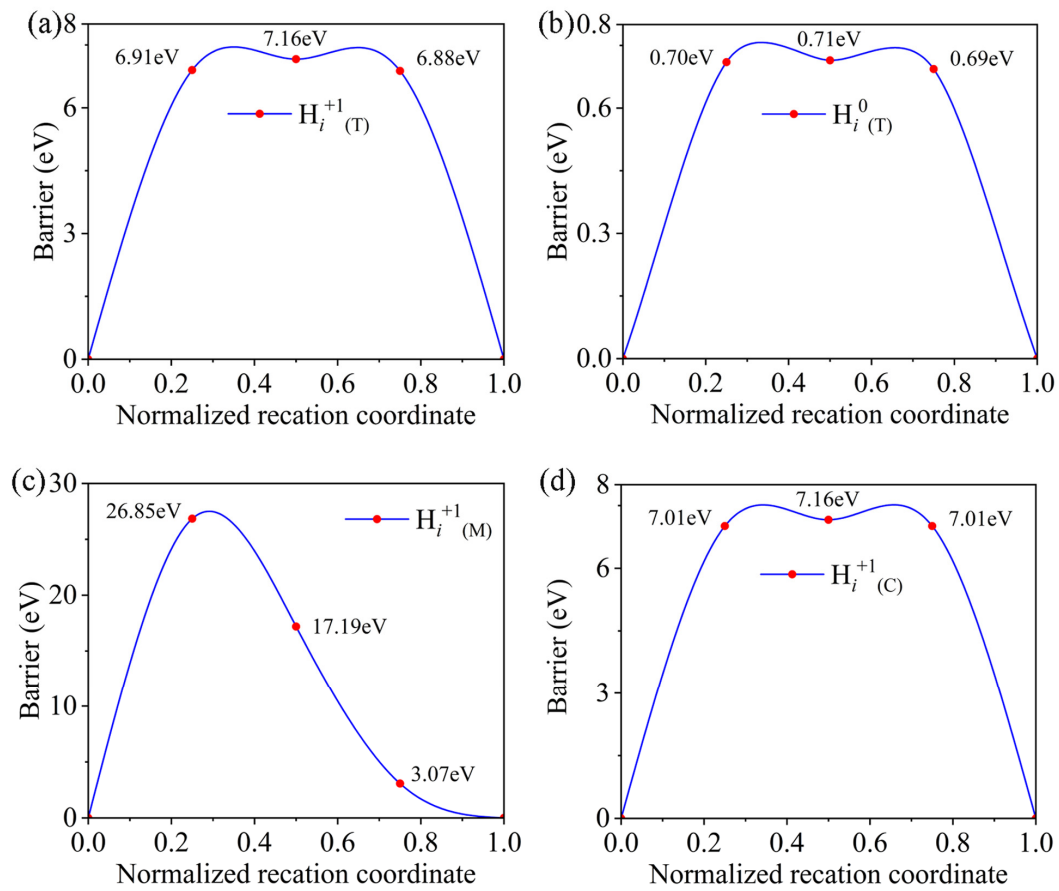


Figure S6 The diffusion barriers of $H_{i(T)}^{+1}$, $H_{i(T)}^0$, $H_{i(M)}^{+1}$ and $H_{i(C)}^{+1}$

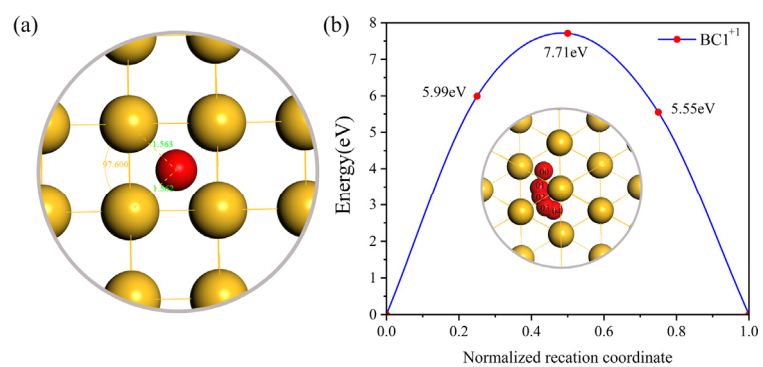


Figure S7 Oxygen at BC1 Sites in c-Si(a), diffusion pathways and diffusion barrier of O^{+1} interstitials defect form BC1 site to the nearest BC1 site (b)

Reference

1. University, P.S., *Introduction to Inorganic Chemistry*. 2024.